JHEP

Published for SISSA by Springer

Received: January 7, 2014
Accepted: March 1, 2014
Published: April 1, 2014

Disentangling Higgs-top couplings in associated production

John Ellis,[a,b] **Dae Sung Hwang,**[c] **Kazuki Sakurai**[a] **and Michihisa Takeuchi**[a]

[a] *Theoretical Particle Physics and Cosmology Group, Physics Department, King's College London, London WC2R 2LS, U.K.*

[b] *TH Division, Physics Department, CERN, CH-1211 Geneva 23, Switzerland*

[c] *Department of Physics, Sejong University, Seoul 143-747, South Korea*

E-mail: John.Ellis@cern.ch, dshwang@sejong.ac.kr, kazuki.sakurai@desy.de, michihisa.takeuchi@kcl.ac.uk

Abstract: In the presence of CP violation, the Higgs-top coupling may have both scalar and pseudoscalar components, κ_t and $\tilde{\kappa}_t$, which are bounded indirectly but only weakly by the present experimental constraints on the Higgs-gluon-gluon and Higgs-γ-γ couplings, whereas upper limits on electric dipole moments provide strong additional indirect constraints on $\tilde{\kappa}_t$, if the Higgs-electron coupling is similar to that in the Standard Model and there are no cancellations with other contributions. We discuss methods to measure directly the scalar and pseudoscalar Higgs-top couplings by measurements of Higgs production in association with $\bar{t}t$, single t and single $\bar{t}$ at the LHC. Measurements of the total cross sections are very sensitive to variations in the Higgs-top couplings that are consistent with the present indirect constraints, as are invariant mass distributions in $\bar{t}tH$, tH and $\bar{t}H$ final states. We also investigate the additional information on κ_t and $\tilde{\kappa}_t$ that could be obtained from measurements of the longitudinal and transverse t polarization in the different associated production channels, and the $\bar{t}t$ spin correlation in $\bar{t}tH$ events.

Keywords: Phenomenological Models, Hadronic Colliders

ArXiv ePrint: 1312.5736

doi:10.1007/JHEP04(2014)004

JHEP04(2014)004

Contents

JHEP04(2014)004

1 Introduction

It is important to characterize the new boson H discovered by the ATLAS [1] and CMS [2] Collaborations. In this paper we refer to this particle as a Higgs boson, since it has some of the expected properties, though others remain to be verified. Tests via H decays into $\gamma\gamma$ [3], WW^* [4] and ZZ^* [5, 6] are consistent with it having spin zero [7–12], as are measurements of H production in association with W and Z [13–15]. In particular, these tests exclude graviton-like spin-two couplings with a high degree of confidence. Assuming that the H spin is indeed zero, the next question is whether it has scalar and/or pseudoscalar couplings.

Tests in WW^* and ZZ^* final states [5–8, 16–20] and production in association with W and Z [13–15] also disfavour strongly pure pseudoscalar couplings, but do not yet exclude a substantial pseudoscalar admixture. In the presence of CP violation, the ratios of scalar and pseudoscalar couplings may differ from channel to channel, and it is important to measure them in as many different channels as possible. Strategies to measure a CP-violating admixture in $H \to \tau^+\tau^-$ decays have been proposed [21–23], and other tests are possible in H production in vector-boson fusion [24–28], double-diffractive [29, 30] and $\gamma\gamma$ collisions [31].

There are already indirect constraints on the scalar and pseudoscalar H-top couplings κ_t and $\tilde{\kappa}_t$ from experimental information on the H-gluon-gluon and H-γ-γ couplings [32], but these constraints are relatively weak [53], as we discuss later. Upper limits on electric

dipole moments also impose important indirect constraints on a possible pseudoscalar H-top coupling $\tilde{\kappa}_t$ [32], if one assumes that if the Higgs-electron coupling is similar to that in the Standard Model and there are no cancellations with other contributing mechanisms.

In this paper we investigate the potential for disentangling scalar and pseudoscalar H-top couplings directly at the LHC, using measurements of H production in association with $\bar{t}t$, single t and single $\bar{t}$. These processes offer many observables that can contribute to determining κ_t and $\tilde{\kappa}_t$, including the total cross sections, $\bar{t}tH$, tH and $\bar{t}H$ invariant mass distributions and various $t(\bar{t})$ polarization observables. These include polarizations both within and perpendicular to the production plane. The latter are particularly interesting, since they violate CP explicitly.

The search strategy for the $\bar{t}tH$ process has been studied in various Higgs decay modes: $\bar{b}b$ [33–35], $\tau\tau$ [36, 37] and WW^* [38–40]. ATLAS [41, 42] and CMS [43–45] have searched for this process intensively using the 8 TeV data set, but the current luminosity and analyses have not reached the sensitivity required by the Standard Model Higgs boson. The associated production of the Higgs and a single top has recently attracted attention since there is a large destructive interference between two Feynman diagrams with $\bar{t}tH$ and WWH couplings in the Standard Model and the production cross section is sensitive to the deviation of the couplings from the the Standard Model values. The dependences on these couplings of the cross section and Higgs branching ratios as well as the search strategy have been studied in [46–50] assuming CP-conserving interactions.

The structure of this paper is as follows. In section 2 we introduce the scalar and pseudoscalar H-top couplings κ_t and $\tilde{\kappa}_t$ and discuss the current indirect experimental constraints, paying particular attention to those provided by LHC constraints on the H-gluon-gluon and H-γ-γ couplings, taking their correlations into account [53]. Section 3 presents calculations of the total cross sections for H production in association with $\bar{t}t$, single t and single $\bar{t}$. We show that, within the region of the $(\kappa_t, \tilde{\kappa}_t)$ plane allowed at the 68% CL, the total cross section for $\bar{t}tH$ production may be considerably *smaller* than in the Standard Model, whereas the cross sections for tH and $\bar{t}H$ may be considerably *larger*. As we show in section 4, the $\bar{t}tH$, tH and $\bar{t}H$ invariant mass distributions may also be very different from those expected in the Standard Model. We proceed in section 5 to discuss the possibilities for t polarization measurements at the LHC.

Our results indicate that the LHC operating at 13/14 TeV may soon be able to provide interesting direct constraints on κ_t and $\tilde{\kappa}_t$, including direct constraints on CP violation in the top sector.

2 Indirect constraints on top-Higgs couplings

We write the top-H couplings in the form

$$\mathcal{L}_t \;=\; -\frac{m_t}{v}\left(\kappa_t \bar{t}t + i\tilde{\kappa}_t \bar{t}\gamma_5 t\right) H\,, \tag{2.1}$$

where $v = 246\,\text{GeV}$ is the conventional Higgs vacuum expectation value (v.e.v.) and $\kappa_t = 1$ and $\tilde{\kappa}_t = 0$ in the Standard Model.

JHEP04(2014)004

As observed in [32], the $\tilde{\kappa}_t$ coupling makes an important contribution to the electric dipole moment of the electron d_e via a two-loop diagram of the Barr-Zee type. Assuming that the H coupling to the electron is the same as in the Standard Model, and that there are no other significant contributions to d_e, the recent upper bound $|d_e/e| < 8.7 \times 10^{-29}$ cm [54] can be used to set the indirect constraint $|\tilde{\kappa}_t| < 0.01$. However, we note that there is no experimental information on the electron-H coupling, that no direct information on this couplings is likely to become available in the foreseeable future, and that there could in principle be other contributions to d_e that might cancel the two-loop top contribution, e.g., in supersymmetric models. We therefore seek bounds on κ_t and $\tilde{\kappa}_t$ that are less model-dependent.

As already commented in the Introduction, the data from ATLAS and CMS on H production at the LHC with $E_{CM} = 7$ and 8 TeV provide indirect bounds on the coupling parameters κ_t and $\tilde{\kappa}_t$ via the constraints they impose on the H-gluon-gluon and H-γ-γ couplings, which have also been explored in [32, 51]. The interpretation of the H-gluon-gluon and H-γ-γ constraints is also somewhat model-dependent, since they are obtained from data on H production and decay into $\gamma\gamma$ final states, and must rely on assumptions about the H couplings to other particles. In considering these constraints, we assume here that the couplings to other fermions and bosons are the same as in the Standard Model, i.e., $\kappa_f = 1$ and $\tilde{\kappa}_f = 0$ for $f \neq t$, and $\kappa_W = \kappa_Z = 1$. This assumption is purely phenomenological but motivated by the following reasons. There are several processes which can constrain κ_W and κ_Z independently from κ_t and $\tilde{\kappa}_t$ [52] at the time when the luminosity required in this study is accumulated. The effect of κ_f and $\tilde{\kappa}_f$ ($f \neq t$) is almost negligible unless $\kappa_f \gg 1$ because of the suppression proportional to the Yukawa couplings of the light fermions. Moreover such a possibility will be ruled out for the bottom and tau by the relatively precise $H \to \bar{b}b$ and $H \to \tau\tau$ measurements available at the time.

Under these assumptions, the available ATLAS and CMS data on H production and decay were analyzed in [53] and constraints on the H-gluon-gluon and H-γ-γ couplings were derived, taking into account the correlations imposed by the measurements: see the left panel of figure 4 of [53]. The ratios

$$\mu_{gg} \equiv \frac{\sigma(gg \to H)}{\sigma(gg \to H)_{\rm SM}}, \quad \mu_{\gamma\gamma} \equiv \frac{\Gamma(H \to \gamma\gamma)}{\Gamma(H \to \gamma\gamma)_{\rm SM}} \tag{2.2}$$

are represented there by c_g^2 and c_γ^2, respectively. Including the contribution to the Hgg loop amplitude of the b quark and the contribution to the $H\gamma\gamma$ loop amplitude of the b quark, τ lepton and W bosons, following [32] one has in the notation of [53]

$$\begin{aligned} c_g^2 &= \mu_{gg} \simeq \kappa_t^2 + 2.6\tilde{\kappa}_t^2 + 0.11\kappa_t(\kappa_t - 1)\,, \\ c_\gamma^2 &= \mu_{\gamma\gamma} \simeq (1.28 - 0.28\kappa_t)^2 + (0.43\tilde{\kappa}_t)^2\,. \end{aligned} \tag{2.3}$$

The left panel of figure 4 of [53] displays regions in the (c_γ, c_g) plane that are allowed by the LHC data at the 68, 95 and 99% CL. There we see explicitly the anticorrelation between c_g and c_γ due to the fact that one may, to some extent, compensate for a possible enhancement

JHEP04(2014)004

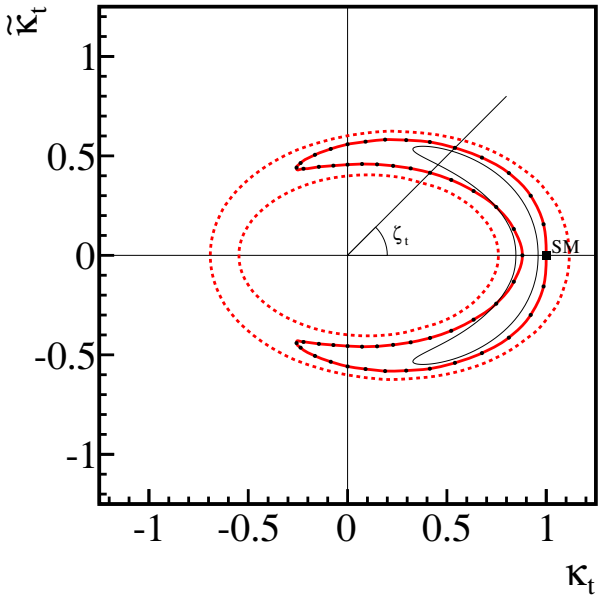

Figure 1. The regions of the $(\kappa_t, \tilde{\kappa}_t)$ plane allowed by the analysis of [53] at the 68 and 95% CL (solid and dotted red contours, respectively). Also shown for comparison is the region discussed in [32] (solid black contour). Black dots represent the simulated model points.

in the LHC $H \to \gamma\gamma$ signal[1] by suppressing $\sigma(gg \to H)$, though this possibility is restricted by the LHC measurements of the strengths of the other H signatures if one assumes that $\kappa_f = 1$ and $\tilde{\kappa}_f = 0$ for $f \neq t$, and $\kappa_W = \kappa_Z = 1$ as done here.

We display in figure 1 the regions of the $(\kappa_t, \tilde{\kappa}_t)$ plane that are allowed at the 68, and 95% CL according to the analysis of [53]. At the 68% CL, the allowed region is a crescent with apex close to the Standard Model point $(\kappa_t, \tilde{\kappa}_t) = (1, 0)$, bounded by the solid red contour, whereas at the 95% CL a complete annulus is allowed, bounded by the dotted red contour. For convenience we define the CP violation phase in the $\bar{t}tH$ coupling by

$$\zeta_t \equiv \arctan\left(\frac{\tilde{\kappa}_t}{\kappa_t}\right). \tag{2.4}$$

For comparison, we also display the (smaller) crescent discussed in [32, 51], bounded by the solid black contour. As already mentioned, if one assumes the Standard Model value of the electron-H coupling and there are no other important contributions to the EDM of the electron d_e, the experimental upper limit on its value imposes $|\tilde{\kappa}_t| < 0.01$. Here we consider the capability of future LHC measurements to constrain κ_t and $\tilde{\kappa}_t$ directly, considering for illustration the full crescent allowed by the analysis of [53] at the 68% CL.

[1] We recall that this possibility is suggested by the ATLAS data, but not by the CMS data, so that the Standard Model value of the $H\gamma\gamma$ coupling is allowed at the 68% CL [53].

JHEP04(2014)004

3 Total cross sections

We have simulated the production of $\bar{t}tH$, tH and $\bar{t}H$ final states at the LHC in leading order[2] using `MadGraph` [55]. All the results presented below are for a centre-of-mass energy of 14 TeV. We consider first the effects on the total cross sections for H production in association with $\bar{t}t$, single t and single $\bar{t}$, taking into account the present LHC constraints discussed in the previous section, and discuss other possible LHC measurements in subsequent sections.

3.1 Cross sections for $\bar{t}tH$ production

The leading tree-level diagrams for $\bar{t}tH$ production at the LHC are displayed in the upper panel of figure 2, and the left panel of figure 3 displays the corresponding values of $\sigma(\bar{t}tH)$ at the LHC at 14 TeV, using colour-coding to represent the ratio to the Standard Model cross section. The contributions of the $\bar{t}tH$ and $\bar{t}\gamma_5 tH$ couplings to $\sigma(\bar{t}tH)$ do not interfere, so the iso-σ contours are ellipses in the $(\kappa_t, \tilde{\kappa}_t)$ plane. For equal values of κ_t and $\tilde{\kappa}_t$, the latter yields a smaller cross section, with the result that the major axes of these ellipses are aligned with the $\tilde{\kappa}_t$ axis, as seen in the left panel of figure 3. Also shown there is the crescent-shaped region allowed by the present LHC data at the 68% CL. It is clear that in this region $\sigma(\bar{t}tH)$ is in general *smaller* than in the Standard Model, as we discuss in more detail later.

The left panel of figure 4 displays the variation of the ratio $\sigma(\bar{t}tH)/\sigma(\bar{t}tH)_{\rm SM}$ along the boundary of the 68% CL crescent displayed in figure 1. The horizontal axis is the CP violation phase, ζ_t, which parametrizes the boundary, and the upper and lower lines correspond to the outer and inner boundaries of the crescent, respectively. We see that an LHC measurement of $\sigma(\bar{t}tH)$ could in principle put an interesting constraint on ζ_t. For example, a measurement at the Standard Model level with an accuracy of 20%, indicated by the horizontal lines in the left panel of figure 4, would determine $\zeta_t \sim 0 \pm 30^o$.

3.2 Cross sections for tH and $\bar{t}H$ production

We now discuss the total cross sections for the associated production of H with a single t or $\bar{t}$ and a light-quark jet via the tree-level diagrams shown in the lower panel of figure 2. We neglect s-channel $\bar{q}q \to tH\bar{b}$ and $\bar{t}Hb$ production, since their cross sections are an order of magnitude smaller than the processes with light quarks [46–49]. In figure 2, we note that H may be radiated from either a final-state t quark or an intermediate virtual W boson. It has been noticed previously that the interference between these diagrams is sensitive to the relative magnitude and sign of the scalar $\bar{t}tH$ and WWH couplings, with the result that $\sigma(tH)$ and $\sigma(\bar{t}H)$ are minimized around the Standard Model value $\kappa_t = 1$ [46–49].[3]

[2] Evaluating NLO corrections lies beyond the scope of this work, but we do not expect them to alter qualitatively the results found here.

[3] Disturbing the $\bar{t}tH$ coupling modifies the UV behaviour of the theory and may lead to a violation of the perturbative unitarity at some scale $\Lambda_{\rm UV}$. It has been shown in [50] that this effect is most pronounced at $\kappa_t = -1$ but $\Lambda_{\rm UV} \gtrsim 9$ TeV even in that case. This implies that the perturbative calculation used in our paper is still reliable.

JHEP04(2014)004

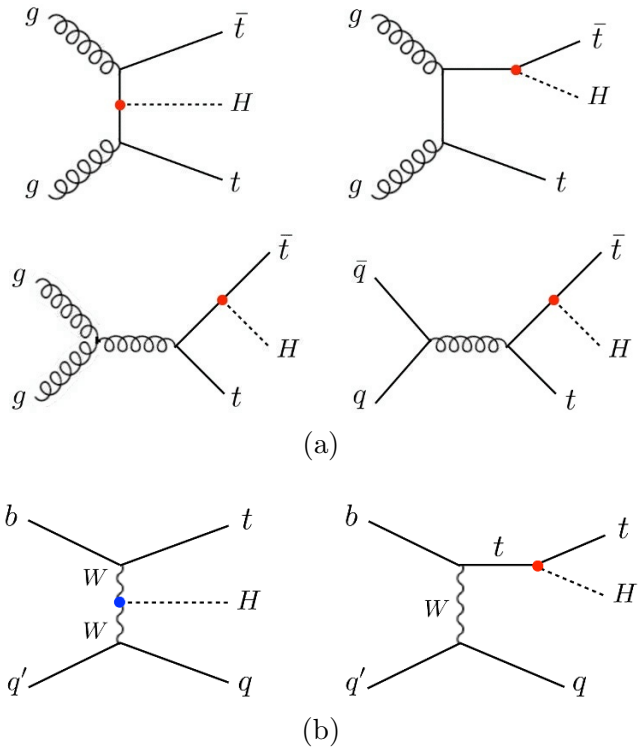

Figure 2. Leading diagrams contributing to $\bar{t}tH$ production at the LHC (upper panel) and to single t or $\bar{t}$ production (lower panel). The red and blue dots correspond to the $\bar{t}tH$ and WWH couplings, respectively.

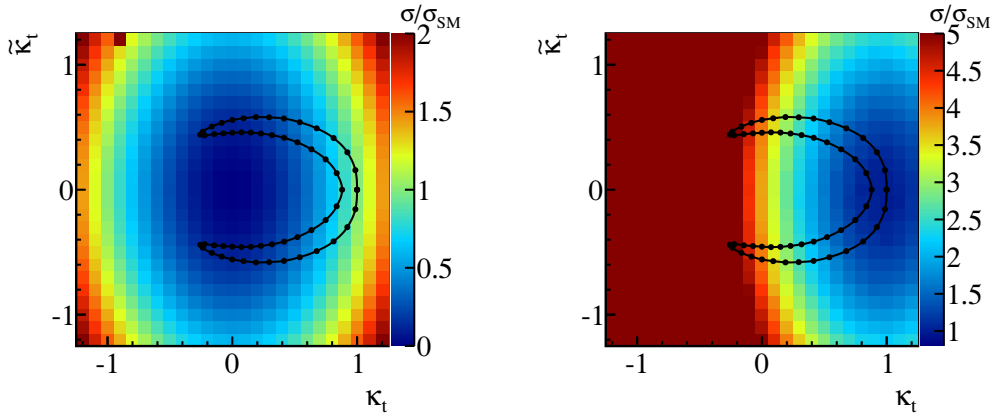

Figure 3. The ratios of $\sigma(\bar{t}tH)$ to the Standard Model value (left panel) and of $\sigma(tH)$ to the Standard Model value (right panel) are shown using the indicated colour codes. Also shown is the crescent-shaped region in figure 1 that is allowed by present data at the 68% CL.

As in the case of $\sigma(\bar{t}tH)$, iso-σ contours for tH and $\bar{t}H$ production are also ellipses whose major axes are aligned with the $\tilde{\kappa}_t$ axis, as we see in the right panel of figure 3, where colour-coding is used to represent the ratio to the Standard Model cross section. As a consequence, $\sigma(tH)$ and $\sigma(\bar{t}H)$ *increase* along the 68% CL crescent as κ_t decreases and $\tilde{\kappa}_t$ increases in magnitude.

JHEP04(2014)004

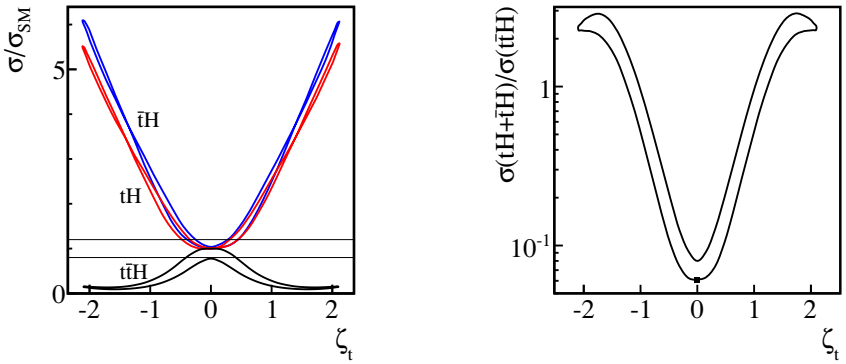

Figure 4. Left panel: the ratios $\sigma(\bar{t}tH)/\sigma(\bar{t}tH)_{\rm SM}$ (black lines), $\sigma(tH)/\sigma(tH)_{\rm SM}$ (red lines) and $\sigma(\bar{t}H)/\sigma(\bar{t}H)_{\rm SM}$ (blue lines) as functions of $\arctan(\tilde{\kappa}_t/\kappa_t)$. Right panel: the ratio $\sigma(tH) + \sigma(\bar{t}H)/\sigma(\bar{t}tH)$ as a function of $\arctan(\tilde{\kappa}_t/\kappa_t)$. In both panels, we display the values of the ratios along both the inner and outer boundaries of the crescent-shaped region in figure 1 that is allowed by present data at the 68% CL. The horizontal lines in the left panel correspond to a measurement of the cross section for $\bar{t}tH$ at the Standard Model level with an accuracy of 20%.

This effect is also seen clearly in the left panel of figure 4, where we see that $\sigma(tH)$ and $\sigma(\bar{t}H)$ reach more than 3 times the Standard Model values when $\zeta_t > 60^o$. A measurement at the Standard Model level with a factor of two uncertainty would determine $\zeta_t \sim 0 \pm 45^o$. As seen in the right panel of figure 4, the combination of the decrease in $\sigma(\bar{t}tH)$ and the increases in $\sigma(tH)$ and $\sigma(\bar{t}H)$ along the crescent imply that the ratio $\sigma(tH + \bar{t}H)/\sigma(\bar{t}tH)$ increases by a factor of more than 20 along the crescent, compared to its value in the Standard Model, ~ 0.06.

4 Mass distributions

We now examine the information that can be obtained from measurements of the invariant masses of combinations of the final-state t, $\bar{t}$ and H particles. In the case of the $\bar{t}tH$ final state, there are three distinct combinations that can be measured: the total invariant mass $M_{\bar{t}tH}$, the tH (or $\bar{t}H$) invariant mass M_{tH} (or $M_{\bar{t}H}$), and the $\bar{t}t$ invariant mass $M_{\bar{t}t}$. In the case of single t or $\bar{t}$ production, there is also a forward jet j corresponding to the quark from which the virtual W was emitted, as seen in the lower panel of figure 2. Hence there are again three final-state particles t (or $\bar{t}$), H and j, and therefore four measurable invariant masses in this case: the total invariant mass M_{tHj} (or $M_{\bar{t}Hj}$) and the two-particle invariant masses M_{tH} (or $M_{\bar{t}H}$), M_{tj} (or $M_{\bar{t}j}$), and M_{Hj}. In the following we present some invariant mass distributions for the $\bar{t}tH$ and tHj (or $\bar{t}Hj$) final states, starting with the total invariant mass distributions. All the distributions shown below are *idealized*, as they do not include the effects of parton showering, object reconstruction, detector resolution, etc. We also do not consider the background contamination and the realistic selection cuts which will be applied in experiments.[4] These effects could alter the shape of distributions, but the study of such effects lies beyond this exploratory work.

[4]The background contamination is known to be a serious problem for the $\bar{t}tH$ process. In addition to improving the techniques to suppress the background, e.g. using jet substructure techniques [33, 34], a precise estimation of the background shapes would be necessary to reduce the systematic uncertainties.

JHEP04(2014)004

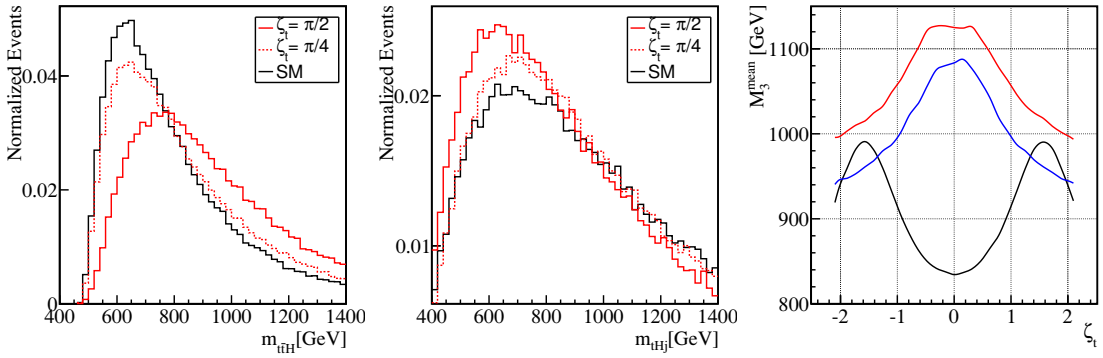

Figure 5. The total invariant mass distributions for the $\bar{t}tH$ final state (left panel) and the tHj final state (central panel). In each case, we display the distributions for $\zeta_t = \arctan(\tilde{\kappa}_t/\kappa_t) = 0$ (in black), $\pm\pi/4$ (in dotted red) and $\pm\pi/2$ (in solid red). The right panel shows the variations with ζ_t of $\langle M_{\bar{t}tH}\rangle$ (solid black), $\langle M_{tHj}\rangle$ (solid red) and $\langle M_{\bar{t}Hj}\rangle$ (solid blue) along a contour passing trough the middle of the 68% CL. crescent-shape allowed region in figure 1.

4.1 Total invariant mass distributions

The left panel of figure 5 displays the normalized $M_{\bar{t}tH}$ distributions for $\zeta_t = \arctan(\tilde{\kappa}_t/\kappa_t) = 0$ (in black), $\pm\pi/4$ (in dotted red) and $\pm\pi/2$ (in solid red). We see that the $M_{\bar{t}tH}$ distribution that is *most* peaked towards small masses is that for the Standard Model case $\zeta_t = 0$. That for $\zeta_t = \pm\pi/4$ is less peaked, and that for $\zeta_t = \pm\pi/2$ is substantially broader.

The central panel of figure 5 displays the M_{tHj} distributions for $\zeta_t = 0, \pm\pi/4$ and $\pm\pi/2$ using the same colour-coding. In this case, we see that the invariant mass distribution is *least* peaked for the Standard Model case $\zeta_t = 0$, more peaked for $\zeta_t = \pm\pi/4$ and particularly for $\zeta_t = \pm\pi/2$.

The right panel of figure 5 displays the variations with ζ_t of $\langle M_{\bar{t}tH}\rangle$ (solid black), $\langle M_{tHj}\rangle$ (solid red) and $\langle M_{\bar{t}Hj}\rangle$ (solid blue). We see explicitly that $\langle M_{\bar{t}tH}\rangle$ is *minimized* in the Standard Model case, whereas $\langle M_{tHj}\rangle$ and $\langle M_{\bar{t}Hj}\rangle$ are *maximized* in this case. These features are correlated with the behaviours of the total cross sections for these processes as functions of ζ_t. We note that $\langle M_{\bar{t}tH}\rangle$ is *maximized* for $|\zeta_t| = \pi/2$: the value for $|\zeta_t| = \pi$ would be the same as in the Standard Model.

4.2 Two-particle invariant mass distributions

More information may be obtained from two-particle invariant mass distributions, and we start by showing the two-body mass distributions in $\bar{t}tH$ production events. The left and central panels of figure 6 show the invariant mass distributions of $\bar{t}t$ and tH, respectively, with the same colour-coding as in figure 5. The peak positions of the distributions are lowest for the SM and highest for $\zeta_t = \pm\pi/2$ in both the $\bar{t}t$ and tH cases. The right panel of figure 6 shows the variation with ζ_t of $\langle M_{\bar{t}t}\rangle$ (solid black) and $\langle M_{tH}\rangle$ (solid red) along a contour passing trough the middle of the crescent-shape allowed region in figure 1. The means of the two-particle invariant mass distributions take their *lowest* values in the Standard Model case and their *maximum* values for $\zeta_t = \pm\pi/2$ in both the $\bar{t}t$ and tH cases, as observed in the total invariant mass distribution. The difference between $\langle M_{\bar{t}t}\rangle$

JHEP04(2014)004

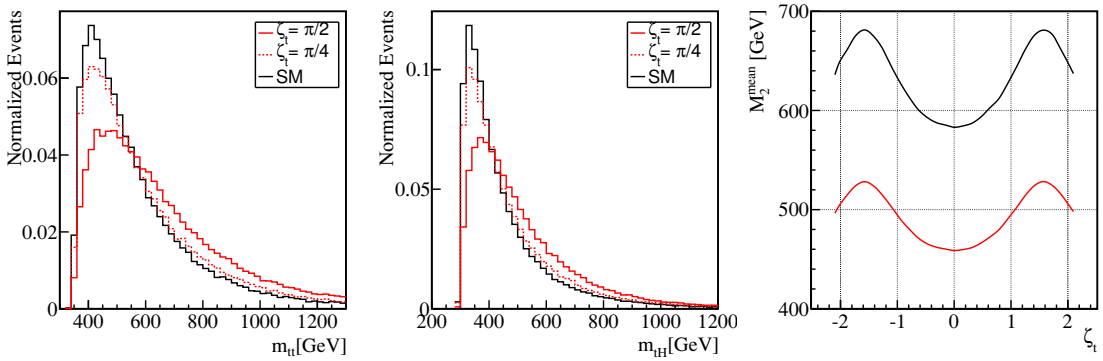

Figure 6. The invariant mass distributions of $\bar{t}t$ (left panel) and tH (central panel) in $\bar{t}tH$ production events. In each case, we display the distributions for $\zeta_t = \arctan(\tilde{\kappa}_t/\kappa_t) = 0$ (in black), $\pm\pi/4$ (in dotted red) and $\pm\pi/2$ (in solid red). The right panel shows the variations with ζ_t of $\langle M_{\bar{t}t}\rangle$ (solid black) and $\langle M_{tH}\rangle$ (solid red) along a contour passing trough the middle of the 68% CL. crescent-shape allowed region in figure 1.

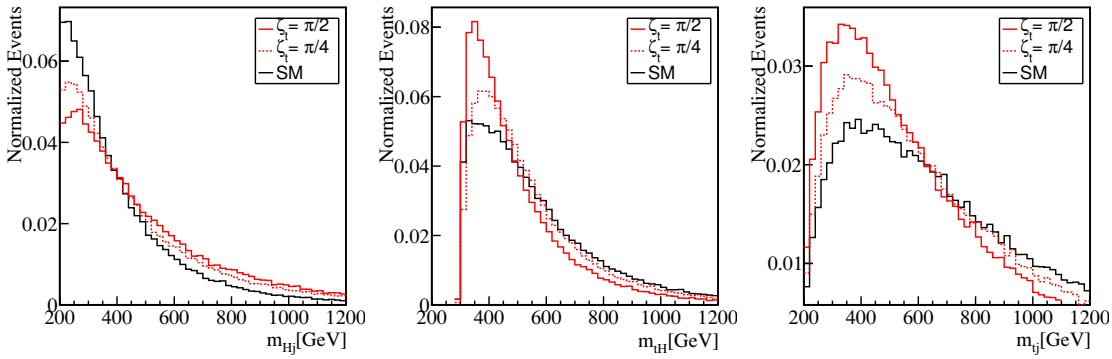

Figure 7. The invariant mass distributions of Hj (left panel), tH (central panel) and tj (right panel) in tHj production events. The black solid, red dashed and red solid histograms correspond to $|\zeta_t| = |\arctan\tilde{\kappa}/\kappa| = 0, \pi/4$ and $\pi/2$.

and $\langle M_{tH}\rangle$ is more than 100 GeV, despite the difference between m_t and m_H being less than 50 GeV, and is almost independent of ζ_t. We do not show the $\bar{t}H$ invariant mass distribution as it is identical to that for tH.

We now turn to the two-particle invariant mass distributions in the tHj and $\bar{t}Hj$ production events. The left, central and right panels of figure 7 show the Hj, tH and tj invariant mass distributions, respectively. In the Hj case, the two-body invariant mass distribution is *most* peaked in the Standard Model case $\zeta_t = 0$, whereas for tH and tj, the distributions are *least* peaked in the Standard Model case and *most* peaked for $|\zeta_t| = \pm\pi/2$, as observed in the total invariant mass distribution.

The left panel of figure 8 shows the variation with ζ_t of $\langle M_{Hj}\rangle$ (dotted black), $\langle M_{tH}\rangle$ (solid red) and $\langle M_{tj}\rangle$ (dotted red) along a contour passing trough the middle of the crescent-shape allowed region. Here we explicitly see $\langle M_{tH}\rangle$ and $\langle M_{tj}\rangle$ are *maximised* for the Standard Model case, whilst $\langle M_{Hj}\rangle$ is *minimized* in this case. Although the threshold of

JHEP04(2014)004

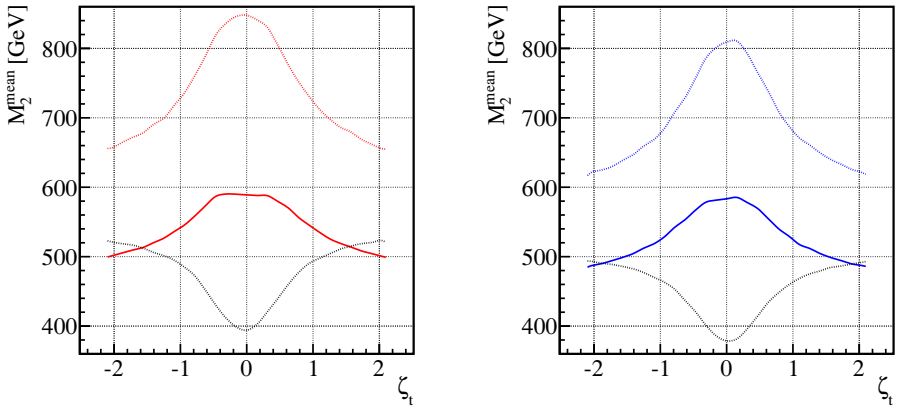

Figure 8. The mean values for the two-body invariant mass distributions in the tHj and $\bar{t}Hj$ final states (left and right panel, respectively) as functions of ζ_t. The values of $\langle M_{Hj}\rangle$ are indicated by dotted black lines, the values of $\langle M_{tH}\rangle$ and $\langle M_{\bar{t}H}\rangle$ are indicated by solid coloured lines (red and blue, respectively), and the values of $\langle M_{tj}\rangle$ and $\langle M_{\bar{t}j}\rangle$ are indicated by dotted coloured lines.

the tj invariant mass is smaller than that for the tH invariant mass, $\langle M_{tj}\rangle$ is larger than $\langle M_{tH}\rangle$ and is indeed the largest among the three two-particle invariant masses in the 68% CL allowed region. In the Standard Model case, $\langle M_{Hj}\rangle$ is smaller than $\langle M_{tH}\rangle$. However this relation becomes reversed near the two tips of the crescent-shape allowed region because of the increase and decrease in $\langle M_{Hj}\rangle$ and $\langle M_{tH}\rangle$, respectively, as ζ_t deviates from the Standard Model value.

We also show the variation with ζ_t of $\langle M_{Hj}\rangle$ (dotted black), $\langle M_{\bar{t}H}\rangle$ (solid blue) and $\langle M_{\bar{t}j}\rangle$ (dotted blue) in $\bar{t}Hj$ production events in the right panel of figure 8. As can be seen, the features we have discussed above for the tHj events are also found for $\bar{t}Hj$ production events. However, we also note a tendency for the two-particle invariant masses in $\bar{t}Hj$ production events to be somewhat smaller than the corresponding invariant masses in tHj production events. This can be traced back to the different initial-state parton distributions involved in tHj and $\bar{t}Hj$ production.

5 Top polarization measurements

We now consider the additional information on the top-H couplings that could be obtained from measurements of the top-(anti)quark polarization(s). In principle, there are two classes of measurements: single-spin measurements in $\bar{t}tH$ and single tH ($\bar{t}H$) production with an accompanying light-quark jet, and measurements of spin-correlations in $\bar{t}tH$ production. Further, one can measure the single-(anti)top polarization either in the production plane or perpendicular to it. The latter is particularly interesting, as it violates CP at the tree level.

5.1 Single-spin measurements

It is easy to see that the single-spin asymmetries actually vanish in $\bar{t}tH$ production, because of the Dirac matrix factors in the vertices. However, the single-spin measurements are

JHEP04(2014)004

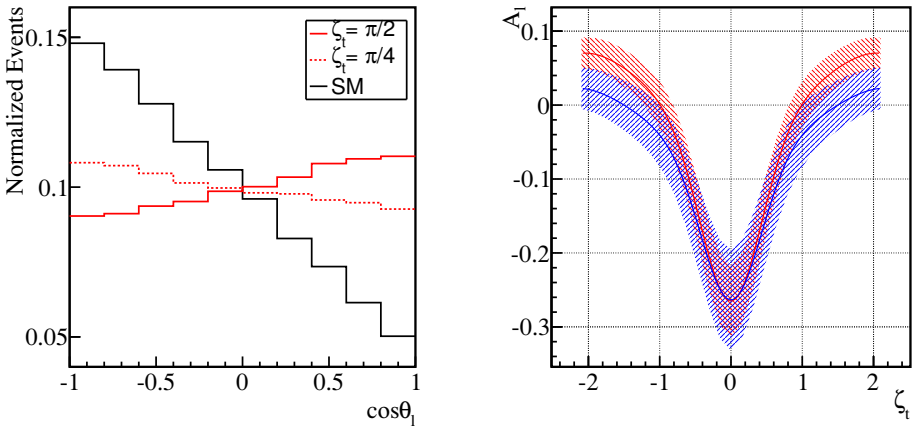

Figure 9. Left panel: the distributions in the semileptonic decay angle θ_ℓ for the tHj final state for the indicated values of ζ_t. In the right panel we display the variation of the forward-backward asymmetry in θ_ℓ, A_l, with ζ_t for tHj ($\bar{t}Hj$) production in red (blue): the shading represents an estimate of the measurement error with 100/fb of integrated luminosity at 14 TeV.

interesting for tHj and $\bar{t}Hj$ production, because of the $1-\gamma_5$ factor in the Wtb coupling. As already noted, the matrix elements of these processes have two competing Feynman diagrams: one is proportional to the WWH coupling and the other to the $\bar{t}tH$ coupling, as seen in the lower panel of figure 2. In the former diagram, the t (or $\bar{t}$) is emitted from the initial $b(\bar{b})$-quark when it exchanges a W boson with a quark (or antiquark) in the other proton. This $t(\bar{t})$ quark therefore prefers the left-handed chirality. In the latter diagram, t (or $\bar{t}$) is produced in the same way but subsequently emits a H, changing its chirality. One can therefore expect that the tops in these processes are polarized to some extent, depending on the details of the $\bar{t}tH$ coupling.

The angular distributions of the top decay products are correlated with the top spin direction in the following way [56–58]:

$$\frac{1}{\Gamma_f}\frac{d\Gamma_f}{d\cos\theta_f} = \frac{1}{2}(1+\omega_f P_t \cos\theta_f)\,, \tag{5.1}$$

where f is the type of top decay product: $f = b, \ell, \ldots$, θ_f is the angle between the decay product f and the top spin quantization axis measured in the rest frame of the top, and P_t is the degree of the top polarization:

$$P_t = \frac{N(\uparrow) - N(\downarrow)}{N(\uparrow) + N(\downarrow)}\,. \tag{5.2}$$

The coefficient ω_f depends on the type of decay product, e.g., $\omega_W = -\omega_b = 0.41$ and $\omega_\ell = 1$ at tree level.

We consider first the angle θ_ℓ between the direction of the t and the final-state lepton ℓ measured at the rest frame of the top in tHj production events. The left panel of figure 9 displays the $\cos\theta_\ell$ distributions. As previously, the distribution for the Standard Model case $\zeta_t = 0$ is shown in black, and the distributions for $|\zeta_t| = \pi/4$ and $\pi/2$ in dotted and

JHEP04(2014)004

solid red, respectively. We can see that the lepton momentum in the Standard Model case strongly prefers the opposite direction to the top's boost direction at the top's rest frame, meaning that tops are negatively polarized, $P_t < 0$. As $|\zeta_t|$ increases this preference is weakend. For $|\zeta_t| = \pi/4$ the distribution is already quite flat, and the slope is even positive, $P_t \gtrsim 0$, for $|\zeta_t| = \pi/2$.

The dependence on ζ_t can more explicitly be seen in the right panel of figure 9, which displays the variation with ζ_t of the forward-backward asymmetry

$$A_\ell = \frac{N(\cos\theta_\ell > 0) - N(\cos\theta_\ell < 0)}{N(\cos\theta_\ell > 0) + N(\cos\theta_\ell < 0)}\,, \tag{5.3}$$

along a contour passing trough the middle of the crescent-shape allowed region. The red and blue curves correspond to the A_ℓ^t and $A_\ell^{\bar{t}}$ in the tHj and $\bar{t}Hj$ production events, respectively. The shaded bands represent estimates of the measurement error with 100/fb of integrated luminosity at 14 TeV, again ignoring effects of parton showering, top reconstruction, detector resolution,[5] etc. We see that, within the range of ζ_t allowed by the present data, the asymmetry is largest in magnitude (and negative) for $\zeta_t = 0$ (the Standard Model case), is reduced in magnitude for $\zeta_t \neq 0$, and changes sign for $\zeta_t = \pm\pi/2$. On the other hand, there is no sensitivity to the sign of ζ_t. In the Standard Model case, the asymmetries for the tHj and $\bar{t}Hj$ events are identical. For $\zeta_t \neq 0$, tops are more positively polarized in the tHj events than in the $\bar{t}Hj$ events.

We now consider the top (anti-top) polarization perpendicular to the three-body production plane. We define the spin quantisation axis by $\vec{p}_j \times \vec{p}_H$ at the rest frame of the top (anti-top), where j is the forward jet produced by the final-state quark after radiating a virtual W in the diagrams in the lower panel of figure 2. The left panel of figure 10 shows the $\cos\theta_{\ell\perp}$ distribution, where $\theta_{\ell\perp}$ is the angle between the lepton momentum and the spin quantization axis defined above at the rest frame of the top. We see that the distribution is flat for the Standard Model case $\zeta_t = 0$. One the other hand, when $\zeta_t \neq 0$, the lepton prefers one side of the hemisphere with respect to the three-body production plane at the rest frame of the top. The right panel in figure 10 shows the variation with ζ_t of the asymmetry $A_{\ell\perp}$, which is defined in the same way as in eq. (5.3) for the $\cos\theta_{\ell\perp}$, with the same colour-coding as in figure 9. As expected, there is no up-down asymmetry for the Standard Model case $\zeta_t = 0$, but there is a measurable asymmetry for $\zeta_t = \pm\pi/4$ and $\pm\pi/2$. In particular, the sign of the perpendicular asymmetry is sensitive to the sign of $\zeta_t = \arctan(\tilde{\kappa}_t/\kappa_t)$. This measurement could therefore provide a direct probe of CP violation in the top-H couplings.

5.2 Spin correlation measurements

We consider finally possible measurements of the $\bar{t}t$ spin correlation in $\bar{t}tH$ production. The left panel of figure 11 shows the distribution in the angle $\Delta\phi_{\ell^+\ell^-}$ between the two lepton momenta projected onto the plane perpendicular to the t direction at the centre-of-mass

[5] For studies including these effects, see e.g. [35, 59, 60].

JHEP04(2014)004

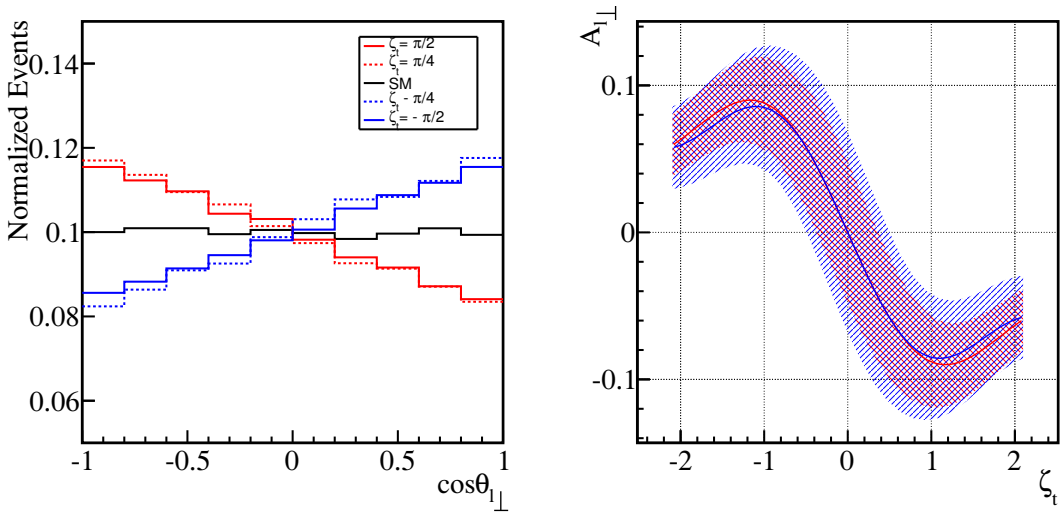

Figure 10. Left panel: the distributions in the semileptonic decay angle $\theta_{\ell\perp}$ out of the tHj plane for $\zeta_t = \arctan(\tilde{\kappa}_t/\kappa_t) = 0$ (in black), $\pm\pi/4$ (in dotted red and blue) and $\pm\pi/2$ (in solid red and blue). Right panel: the asymmetry perpendicular to the plane of tHj ($\bar{t}Hj$) production, $A_{l\perp}$, as a function of ζ_t is indicated in red (blue): the shading represents an estimate of the measurement error with 100/fb of integrated luminosity at 14 TeV.

frame of the $\bar{t}t$ system. The sign of $\Delta\phi_{\ell^+\ell^-}$ is defined as the sign of $\vec{p}_t \cdot (\vec{p}_{\ell^-} \times \vec{p}_{\ell^+})$.[6] As previously, the distribution for the Standard Model case $\zeta_t = \arctan(\tilde{\kappa}_t/\kappa_t) = 0$ is shown in black, those for $\zeta_t = \pm\pi/4$ as dotted lines, and those for $\pm\pi/2$ as solid lines (red and blue for $\zeta_t >, < 0$, respectively). We see that the distribution has the form

$$\frac{d\sigma}{d\Delta\phi_{\ell^+\ell^-}} \propto \cos(\Delta\phi_{\ell^+\ell^-} - \delta) + \text{const.} \tag{5.4}$$

We see in the left panel of figure 11 that the phase shift δ vanishes for the Standard Model case $\zeta_t = 0$, but takes non-zero values for $\zeta_t \neq 0$, and we note that this phase shift is sensitive to the sign of ζ_t. The right panel in figure 11 shows the value of δ as a function of ζ_t. One can see that the δ varies from $-\pi$ to π as ζ_t varies from $-\pi/2$ to $\pi/2$. We find that the dependence of δ on ζ_t can be very well fitted by the function $\delta = 2\zeta_t - \sin(2\zeta_t)/2$.

6 Summary

We have shown in this paper that the cross sections and final-state distributions in $\bar{t}tH$, tH and $\tilde{t}H$ production are sensitive to the ratio between the scalar and pseudoscalar top-H couplings κ_t and $\tilde{\kappa}_t$. In particular, the total cross section for $\bar{t}tH$ production *decreases* significantly as the ratio $\tilde{\kappa}_t/\kappa_t$ *increases* within the ranges of values of these couplings that are allowed by present data on the Hgg and $H\gamma\gamma$ couplings. On the other hand, the total cross sections for tH and $\tilde{t}H$ production *increase* as the ratio $\tilde{\kappa}_t/\kappa_t$ *increases*.

[6] The $\Delta\phi_{\ell^+\ell^-}$ variable is commonly used in the spin correlation measurement in the $\bar{t}t$ process [61, 62], although $\Delta\phi_{\ell^+\ell^-}$ is defined at the lab frame and its range is $[0, \pi]$. In order to identify CP violation, it is crucial to measure $\Delta\phi_{\ell^+\ell^-}$ with respect to the top (or anti-top) axis in the range of $[-\pi, \pi]$.

JHEP04(2014)004

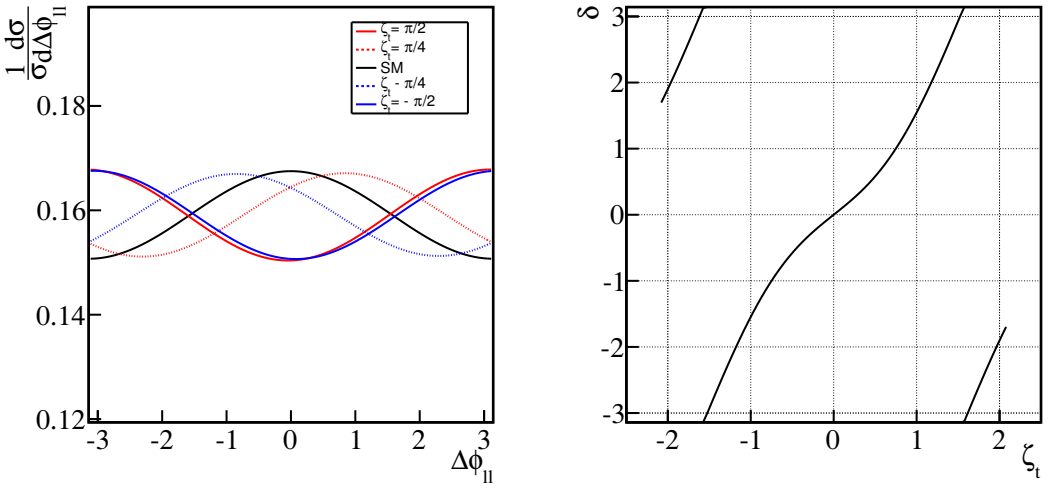

Figure 11. Left panel: the distributions in the angle $\Delta\phi_{\ell^+\ell^-}$ between the leptons produced in t and $\bar{t}$ decay in $\bar{t}tH$ production, in the centre-of-mass of the $\bar{t}t$ system. We display the distributions for $\zeta_t = \arctan(\tilde{\kappa}_t/\kappa_t) = 0$ (in black), $\pm\pi/4$ (in dotted red and blue) and $\pm\pi/2$ (in solid red and blue). Right panel: the phase shift δ as a function of ζ_t.

We have also found that the invariant mass distributions for the three-body combinations $\bar{t}tH$, tHj and $\tilde{t}Hj$ are sensitive to the ratio $\tilde{\kappa}_t/\kappa_t$, becoming *less* peaked at small masses in the $\bar{t}tH$ case and *more* peaked in the tHj and $\tilde{t}Hj$ cases as the ratio $\tilde{\kappa}_t/\kappa_t$ increases. The two-body invariant mass distributions also carry information about the top-H couplings.

Supplementary information on the ratio $\tilde{\kappa}_t/\kappa_t$ could be provided by angular distributions in semileptonic t and $\bar{t}$ decays. In particular, lepton decay angles from the top boost direction could provide information on the *magnitude* of $\tilde{\kappa}_t/\kappa_t$, and lepton decay angles against the tHj (or $\bar{t}Hj$) production plane provide information on the *sign* of $\tilde{\kappa}_t/\kappa_t$. Information both on the *magnitude* and *sign* of $\tilde{\kappa}_t/\kappa_t$ could also be provided by measurements of the angle $\Delta\phi_{\ell^+\ell^-}$ between the directions of leptons produced in $\bar{t}$ and t decays in the case of $\bar{t}tH$ production.

We conclude that there are good prospects for disentangling the scalar and pseudoscalar top-H couplings at the LHC via a combination of measurements of $\bar{t}tH$, tH and $\bar{t}H$ production.

Acknowledgments

The work of J.E. and K.S. was supported in part by the London Centre for Terauniverse Studies (LCTS), using funding from the European Research Council via the Advanced Investigator Grant 267352. J.E. and M.T. are grateful for funding from the Science and Technology Facilities Council (STFC). The work of D.S.H. was supported in part by the Korea Foundation for International Cooperation of Science & Technology (KICOS) and the Basic Science Research Programme through the National Research Foundation of Korea (2013028705).

JHEP04(2014)004

References

[1] ATLAS collaboration, *Observation of a new particle in the search for the Standard Model Higgs boson with the ATLAS detector at the LHC*, *Phys. Lett.* **B 716** (2012) 1 [arXiv:1207.7214] [INSPIRE].

[2] CMS collaboration, *Observation of a new boson at a mass of 125 GeV with the CMS experiment at the LHC*, *Phys. Lett.* **B 716** (2012) 30 [arXiv:1207.7235] [INSPIRE].

[3] ATLAS collaboration, *Study of the spin of the Higgs-like boson in the two photon decay channel using 20.7 fb^{-1} of pp collisions collected at $\sqrt{s} = 8$ TeV with the ATLAS detector*, ATLAS-CONF-2013-029 (2013).

[4] ATLAS collaboration, *Study of the spin properties of the Higgs-like particle in the $H \to WW^{(*)} \to e\nu\mu\nu$ channel with 21 fb^{-1} of $\sqrt{s} = 8$ TeV data collected with the ATLAS detector*, ATLAS-CONF-2013-031 (2013).

[5] ATLAS collaboration, *Measurements of the properties of the Higgs-like boson in the four lepton decay channel with the ATLAS detector using 25 fb^{-1} of proton-proton collision data*, ATLAS-CONF-2013-013 (2013).

[6] CMS collaboration, *Study of the Mass and Spin-Parity of the Higgs Boson Candidate Via Its Decays to Z Boson Pairs*, *Phys. Rev. Lett.* **110** (2013) 081803 [arXiv:1212.6639] [INSPIRE].

[7] S. Bolognesi et al., *On the spin and parity of a single-produced resonance at the LHC*, *Phys. Rev.* **D 86** (2012) 095031 [arXiv:1208.4018] [INSPIRE].

[8] A. Freitas and P. Schwaller, *Higgs CP Properties From Early LHC Data*, *Phys. Rev.* **D 87** (2013) 055014 [arXiv:1211.1980] [INSPIRE].

[9] J. Ellis and D.S. Hwang, *Does the 'Higgs' have Spin Zero?*, *JHEP* **09** (2012) 071 [arXiv:1202.6660] [INSPIRE].

[10] J. Ellis, R. Fok, D.S. Hwang, V. Sanz and T. You, *Distinguishing 'Higgs' spin hypotheses using $\gamma\gamma$ and WW^* decays*, *Eur. Phys. J.* **C 73** (2013) 2488 [arXiv:1210.5229] [INSPIRE].

[11] J. Ellis, V. Sanz and T. You, *Prima Facie Evidence against Spin-Two Higgs Impostors*, *Phys. Lett.* **B 726** (2013) 244 [arXiv:1211.3068] [INSPIRE].

[12] ATLAS collaboration, *Study of the spin of the new boson with up to 25 fb^{-1} of ATLAS data*, ATLAS-CONF-2013-040 (2013).

[13] J. Ellis, D.S. Hwang, V. Sanz and T. You, *A Fast Track towards the 'Higgs' Spin and Parity*, *JHEP* **11** (2012) 134 [arXiv:1208.6002] [INSPIRE].

[14] D0 collaboration, http://www-d0.fnal.gov/Run2Physics/WWW/results/prelim/HIGGS/H138/H138.pdf, http://www-d0.fnal.gov/Run2Physics/WWW/results/prelim/HIGGS/H139/H139.pdf.

[15] J. Ellis, V. Sanz and T. You, *Associated Production Evidence against Higgs Impostors and Anomalous Couplings*, *Eur. Phys. J.* **C 73** (2013) 2507 [arXiv:1303.0208] [INSPIRE].

[16] R.M. Godbole, D. Miller and M.M. Muhlleitner, *Aspects of CP-violation in the H ZZ coupling at the LHC*, *JHEP* **12** (2007) 031 [arXiv:0708.0458] [INSPIRE].

JHEP04(2014)004

[17] Y. Gao et al., *Spin determination of single-produced resonances at hadron colliders*, *Phys. Rev.* **D 81** (2010) 075022 [arXiv:1001.3396] [INSPIRE].

[18] B. Coleppa, K. Kumar and H.E. Logan, *Can the 126 GeV boson be a pseudoscalar?*, *Phys. Rev.* **D 86** (2012) 075022 [arXiv:1208.2692] [INSPIRE].

[19] A. Djouadi and G. Moreau, *The couplings of the Higgs boson and its CP properties from fits of the signal strengths and their ratios at the* $7+8$ *TeV LHC*, arXiv:1303.6591 [INSPIRE].

[20] D. Stolarski and R. Vega-Morales, *Directly Measuring the Tensor Structure of the Scalar Coupling to Gauge Bosons*, *Phys. Rev.* **D 86** (2012) 117504 [arXiv:1208.4840] [INSPIRE].

[21] T. Plehn, D.L. Rainwater and D. Zeppenfeld, *Determining the structure of Higgs couplings at the LHC*, *Phys. Rev. Lett.* **88** (2002) 051801 [hep-ph/0105325] [INSPIRE].

[22] S. Berge, W. Bernreuther, B. Niepelt and H. Spiesberger, *How to pin down the CP quantum numbers of a Higgs boson in its tau decays at the LHC*, *Phys. Rev.* **D 84** (2011) 116003 [arXiv:1108.0670] [INSPIRE].

[23] R. Harnik, A. Martin, T. Okui, R. Primulando and F. Yu, *Measuring CP-violation in* $h \to \tau^+\tau^-$ *at Colliders*, *Phys. Rev.* **D 88** (2013) 076009 [arXiv:1308.1094] [INSPIRE].

[24] K. Hagiwara, Q. Li and K. Mawatari, *Jet angular correlation in vector-boson fusion processes at hadron colliders*, *JHEP* **07** (2009) 101 [arXiv:0905.4314] [INSPIRE].

[25] C. Englert, M. Spannowsky and M. Takeuchi, *Measuring Higgs CP and couplings with hadronic event shapes*, *JHEP* **06** (2012) 108 [arXiv:1203.5788] [INSPIRE].

[26] J.R. Andersen, C. Englert and M. Spannowsky, *Extracting precise Higgs couplings by using the matrix element method*, *Phys. Rev.* **D 87** (2013) 015019 [arXiv:1211.3011] [INSPIRE].

[27] C. Englert, D. Goncalves-Netto, K. Mawatari and T. Plehn, *Higgs Quantum Numbers in Weak Boson Fusion*, *JHEP* **01** (2013) 148 [arXiv:1212.0843] [INSPIRE].

[28] C. Englert, D. Goncalves, G. Nail and M. Spannowsky, *The shape of spins*, *Phys. Rev.* **D 88** (2013) 013016 [arXiv:1304.0033] [INSPIRE].

[29] V. Khoze, A. Martin and M. Ryskin, *Hunting a light CP-violating Higgs via diffraction at the LHC*, *Eur. Phys. J.* **C 34** (2004) 327 [hep-ph/0401078] [INSPIRE].

[30] J.R. Ellis, J.S. Lee and A. Pilaftsis, *Diffraction as a CP and lineshape analyzer for MSSM Higgs bosons at the LHC*, *Phys. Rev.* **D 71** (2005) 075007 [hep-ph/0502251] [INSPIRE].

[31] ECFA/DESY Photon Collider Working Group collaboration, B. Badelek et al., *TESLA: The Superconducting electron positron linear collider with an integrated X-ray laser laboratory. Technical design report. Part 6. Appendices. Chapter 1. Photon collider at TESLA*, *Int. J. Mod. Phys.* **A 19** (2004) 5097 [hep-ex/0108012] [INSPIRE].

[32] J. Brod, U. Haisch and J. Zupan, *Constraints on CP-violating Higgs couplings to the third generation*, *JHEP* **11** (2013) 180 [arXiv:1310.1385] [INSPIRE].

[33] T. Plehn, G.P. Salam and M. Spannowsky, *Fat Jets for a Light Higgs*, *Phys. Rev. Lett.* **104** (2010) 111801 [arXiv:0910.5472] [INSPIRE].

[34] P. Artoisenet, P. de Aquino, F. Maltoni and O. Mattelaer, *Unravelling* $t\bar{t}h$ *via the matrix element method*, *Phys. Rev. Lett.* **111** (2013) 091802 [arXiv:1304.6414] [INSPIRE].

[35] M.R. Buckley, T. Plehn, T. Schell and M. Takeuchi, *Buckets of Higgs and Tops*, *JHEP* **02** (2014) 130 [arXiv:1310.6034] [INSPIRE].

JHEP04(2014)004

[36] C. Boddy, S. Farrington and C. Hays, *Higgs boson coupling sensitivity at the LHC using $H \to \tau\tau$ decays*, *Phys. Rev.* **D 86** (2012) 073009 [arXiv:1208.0769] [INSPIRE].

[37] P. Agrawal, S. Bandyopadhyay and S.P. Das, *Dilepton Signatures of the Higgs Boson with Tau-jet Tagging*, arXiv:1308.6511 [INSPIRE].

[38] F. Maltoni, D.L. Rainwater and S. Willenbrock, *Measuring the top quark Yukawa coupling at hadron colliders via $t\bar{t}H, H \to W^+W^-$*, *Phys. Rev.* **D 66** (2002) 034022 [hep-ph/0202205] [INSPIRE].

[39] D. Curtin, J. Galloway and J.G. Wacker, *Measuring the tth coupling from SSDL+2b measurements*, *Phys. Rev.* **D 88** (2013) 093006 [arXiv:1306.5695] [INSPIRE].

[40] P. Agrawal, S. Bandyopadhyay and S.P. Das, *Multilepton Signatures of the Higgs Boson through its Production in Association with a Top-quark Pair*, *Phys. Rev.* **D 88** (2013) 093008 [arXiv:1308.3043] [INSPIRE].

[41] ATLAS collaboration, *Search for ttH production in the $H \to yy$ channel at $\sqrt{s} = 8$ TeV with the ATLAS detector*, ATLAS-CONF-2013-080 (2013).

[42] ATLAS collaboration, *Search for the Standard Model Higgs boson produced in association with top quarks in proton-proton collisions at $\sqrt{s} = 7$ TeV using the ATLAS detector*, ATLAS-CONF-2012-135 (2012).

[43] CMS collaboration, *Search for ttH production in events where H decays to photons at 8 TeV collisions*, CMS-PAS-HIG-13-015 (2013).

[44] CMS collaboration, *Search for Higgs Boson Production in Association with a Top-Quark Pair and Decaying to Bottom Quarks or Tau Leptons*, CMS-PAS-HIG-13-019 (2013).

[45] CMS collaboration, *Search for the standard model Higgs boson produced in association with top quarks in multilepton final states*, CMS-PAS-HIG-13-020 (2013).

[46] F. Maltoni, K. Paul, T. Stelzer and S. Willenbrock, *Associated production of Higgs and single top at hadron colliders*, *Phys. Rev.* **D 64** (2001) 094023 [hep-ph/0106293] [INSPIRE].

[47] S. Biswas, E. Gabrielli and B. Mele, *Single top and Higgs associated production as a probe of the Htt coupling sign at the LHC*, *JHEP* **01** (2013) 088 [arXiv:1211.0499] [INSPIRE].

[48] P. Agrawal, S. Mitra and A. Shivaji, *Effect of Anomalous Couplings on the Associated Production of a Single Top Quark and a Higgs Boson at the LHC*, *JHEP* **12** (2013) 077 [arXiv:1211.4362] [INSPIRE].

[49] S. Biswas, E. Gabrielli, F. Margaroli and B. Mele, *Direct constraints on the top-Higgs coupling from the 8 TeV LHC data*, *JHEP* **07** (2013) 073 [arXiv:1304.1822] [INSPIRE].

[50] M. Farina, C. Grojean, F. Maltoni, E. Salvioni and A. Thamm, *Lifting degeneracies in Higgs couplings using single top production in association with a Higgs boson*, *JHEP* **05** (2013) 022 [arXiv:1211.3736] [INSPIRE].

[51] K. Nishiwaki, S. Niyogi and A. Shivaji, *ttH Anomalous Coupling in Double Higgs Production*, arXiv:1309.6907 [INSPIRE].

[52] M. Klute, R. Lafaye, T. Plehn, M. Rauch and D. Zerwas, *Measuring Higgs Couplings at a Linear Collider*, *Europhys. Lett.* **101** (2013) 51001 [arXiv:1301.1322] [INSPIRE].

[53] J. Ellis and T. You, *Updated Global Analysis of Higgs Couplings*, *JHEP* **06** (2013) 103 [arXiv:1303.3879] [INSPIRE].

JHEP04(2014)004

[54] ACME collaboration, J. Baron et al., *Order of Magnitude Smaller Limit on the Electric Dipole Moment of the Electron*, *Science* **343** (2014) 269 [arXiv:1310.7534] [INSPIRE].

[55] J. Alwall, M. Herquet, F. Maltoni, O. Mattelaer and T. Stelzer, *MadGraph 5: going beyond*, *JHEP* **06** (2011) 128 [arXiv:1106.0522] [INSPIRE].

[56] M. Jezabek, *Top quark physics*, *Nucl. Phys. Proc. Suppl.* **37B** (1994) 197 [hep-ph/9406411] [INSPIRE].

[57] A. Brandenburg, Z. Si and P. Uwer, *QCD corrected spin analyzing power of jets in decays of polarized top quarks*, *Phys. Lett.* **B 539** (2002) 235 [hep-ph/0205023] [INSPIRE].

[58] R.M. Godbole, K. Rao, S.D. Rindani and R.K. Singh, *On measurement of top polarization as a probe of $t\bar{t}$ production mechanisms at the LHC*, *JHEP* **11** (2010) 144 [arXiv:1010.1458] [INSPIRE].

[59] M.R. Buckley, T. Plehn and M. Takeuchi, *Buckets of tops*, *JHEP* **08** (2013) 086 [arXiv:1302.6238] [INSPIRE].

[60] A. Papaefstathiou and K. Sakurai, *Determining the Helicity Structure of Third Generation Resonances*, *JHEP* **06** (2012) 069 [arXiv:1112.3956] [INSPIRE].

[61] ATLAS collaboration, *Observation of spin correlation in $t\bar{t}$ events from pp collisions at $\sqrt{s} = 7$ TeV using the ATLAS detector*, *Phys. Rev. Lett.* **108** (2012) 212001 [arXiv:1203.4081] [INSPIRE].

[62] CMS collaboration, *Measurement of Spin Correlations in $t\bar{t}$ production*, CMS-PAS-TOP-12-004 (2012).

JHEP04(2014)004